Wave-driven currents and vortex dynamics on barred beaches

By OLIVER BÜHLER[1] AND TIVON E. JACOBSON[2]

[1]School of Mathematics and Statistics, University of St Andrews,
St Andrews KY16 9SS, UK

[2]Courant Institute of Mathematical Sciences, New York, NY University,
New York, NY 10012, USA

We present a theoretical and numerical investigation of longshore currents driven by breaking waves on beaches, especially barred beaches. The novel feature considered here is that the wave envelope is allowed to vary in the alongshore direction, which leads to the generation of strong dipolar vortex structures where the waves are breaking. The nonlinear evolution of these vortex structures is studied in detail using a simple analytical theory to model the effect of a sloping beach. One of our findings is that the vortex evolution provides a robust mechanism through which the preferred location of the longshore current can move shorewards from the location of wave breaking. Such current dislocation is an often-observed (but ill-understood) phenomenon on real barred beaches.

To underpin our results, we present a comprehensive theoretical description of the relevant wave–mean interaction theory in the context of a shallow-water model for the beach. Therein we link the radiation-stress theory of Longuet-Higgins & Stewart to recently established results concerning the mean vorticity generation due to breaking waves. This leads to detailed results for the entire life-cycle of the mean-flow vortex evolution, from its initial generation by wave breaking until its eventual dissipative decay due to bottom friction.

In order to test and illustrate our theory we also present idealized nonlinear numerical simulations of both waves and vortices using the full shallow-water equations with bottom topography. In these simulations wave breaking occurs through shock formation of the shallow-water waves. We note that because the shallow-water equations also describe the two-dimensional flow of a homentropic perfect gas, our theoretical and numerical results can also be applied to nonlinear acoustics and sound–vortex interactions.

1. Introduction

It is well known that the breaking of obliquely incident ocean waves on a beach can generate a current running in the alongshore direction. These longshore currents are a familiar feature of coastal oceanography, and they are recognized to play a rôle, for instance, in sediment transport and beach erosion. A quantitative theory of this phenomenon was first given in Longuet-Higgins (1970*a*,*b*) (hereafter referred to as LH70*a*,*b*) based on the radiation-stress theory for ocean waves developed earlier in a sequence of papers by Longuet-Higgins & Stewart (1960, 1961, 1962, 1963, 1964). In this theory a steady and homogeneous wavetrain is considered, where homogeneous
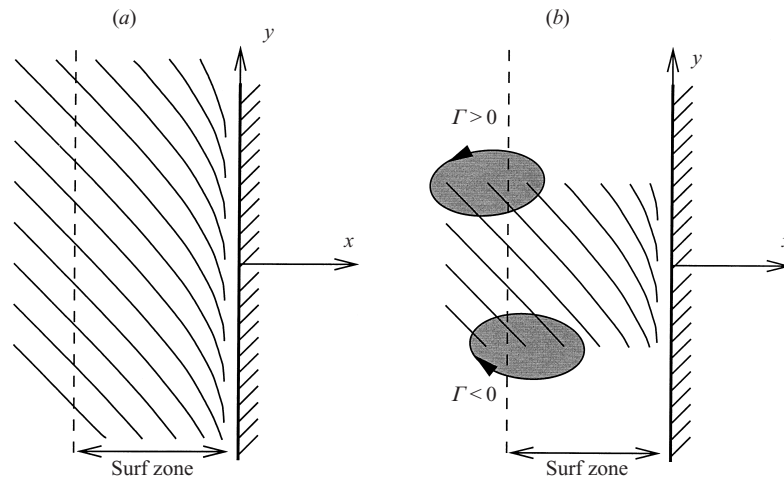
FIGURE 1. (*a*) Phase lines of a homogeneous wavetrain incident on a straight shoreline at $x = 0$ (cf. LH70*a*,*b*), with alongshore coordinate y. The refraction of the waves due to decreasing h_S is indicated, as is the approximate width of the surf zone. (*b*) The inhomogeneous wavetrain considered in the present paper. The wave breaking in the surf zone generates a vortex dipole with oppositely signed circulations $\pm\Gamma$.

means that the wavetrain does not vary in the alongshore direction (see figure 1*a*). The refraction of the waves by the varying still water depth h_S is approximated by ray tracing and the wave breaking in the surf zone is modelled by imposing a suitable saturation amplitude on the waves. The wave breaking leads to a convergence of wave-induced momentum flux and to an effective mean force whose alongshore component drives the current. A smooth profile for the longshore current can then be calculated under the assumption that the momentum-flux convergence due to wave breaking is balanced by bottom friction and by suitably modelled turbulent horizontal mixing. Predictions based on this theory have provided good explanations of field and laboratory data in the case of *planar* beaches, in which the still water depth h_S is a monotonically increasing function of distance from the shoreline.

However, there have been persistent and significant discrepancies between theory and observations in the case of *barred* beaches, in which there is an interior minimum of water depth h_S on a bar crest at some distance from the shoreline (cf. location A in figure 2). The theory then predicts two current maxima, which are correlated with the locations of strongest wave breaking. One maximum occurs near the top of the bar crest (A) and the other occurs near the shoreline (C), where h_S goes to zero. In contrast, barred beach observations often show a single current maximum situated in the trough (B) between the bar crest and the shoreline (e.g. Church & Thornton 1993). This means that the current has been dislocated away from the regions of strongest wave breaking, in contrast with the predictions of the theory in LH70*a*,*b*. Small changes to the theory (such as considering a statistical ensemble of incoming waves, different wave breaking criteria, different models for bottom friction and turbulence, or the *ad-hoc* introduction of delayed momentum flux convergences due to so-called wave 'rollers') have had little impact on resolving this basic discrepancy.

Interestingly, laboratory experiments reported in Reniers & Battjes (1997) broadly confirmed the predictions of the theory for both barred and non-barred beaches, but in these experiments only homogeneous wavetrains were considered. It seems com-
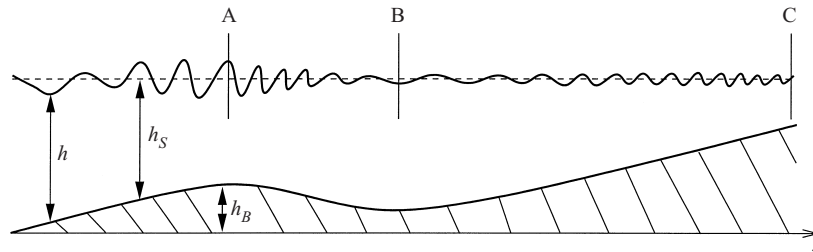
FIGURE 2. Schematic cross-section (with exaggerated vertical scale) of a barred beach showing the fluid layer depth h and the bottom elevation h_B, which add to give the fluid surface height $h + h_B$. Also shown is the still water depth h_S such that $h_S + h_B = $ const. The surface disturbance is then $\Delta h = h - h_S$. In the present paper h_B (and hence h_S) depend only on the offshore coordinate x. Location A denotes the bar crest, B the bar trough, and C the approach to the shoreline. As indicated, the incoming waves steepen and break pre-dominantly over the bar crest.

pelling to hypothesize that the discrepancies should therefore somehow be related to inhomogeneity in the alongshore direction, which is certainly a feature of real surf zones. Such inhomogeneity can arise through alongshore dependence of either h_S or of the waves themselves. Inhomogeneous h_S would necessarily also generate inhomogeneity of the waves. For simplicity we will henceforth consider inhomogeneous wavetrains whilst restricting the still water depth to functions $h_S(x)$.

Now, the mean-flow dynamics in the case of an inhomogeneous wavetrain differs markedly from that in the homogeneous case considered in LH70a, b. Specifically, breaking waves can now generate strong mean-flow vorticity situated at the flanks of the wavetrain (e.g. Peregrine 1998, 1999; Bühler 2000, hereafter referred to as B2000). This is illustrated in figure 1(b). This dipolar vorticity structure can be idealized as a vortex couple and in § 2 we present a study of the nonlinear dynamics of such vortex couples on a sloping beach. In a nutshell, considering the mean-flow vortex dynamics makes it evident that the location of the strongest wave breaking need not coincide with the eventual location of the strongest current. This current dislocation effect occurs even on a planar beach, albeit weakly. However, the effect becomes significant on barred beaches. Indeed, the compelling result of these considerations will be that a bar trough becomes the preferred location for the longshore current on a barred beach.

As far as we are aware, the radiation-stress theory of LH70a, b has not been adapted previously for the case of an inhomogeneous wavetrain. This may be due to two difficulties that arise in this connection. First, in the inhomogeneous case the radiation-stress convergence contains dissipative terms due to wave breaking as well as non-dissipative terms due to mean pressure changes. This makes it harder to identify the dissipative terms, which alone can create mean-flow vorticity because of Kelvin's circulation theorem. We use the recently established results in B2000 (which builds on Andrews & McIntyre 1978 and other related work in atmospheric wave–mean interaction theory) to identify clearly an effective dissipative force within the radiation-stress convergence. This force appears in the pseudomomentum budget of the waves and its curl produces the mean-flow vorticity, which provides the quantitative link between wave dissipation and mean-flow vorticity generation.

The second problem is that a wave-driven longshore current saturates at an amplitude of the same order as the wave amplitude. This means that the nonlinear mean-flow dynamics occurs over an advective time scale that is inversely proportional

to the wave amplitude. A wave–mean interaction theory that is valid over such long, amplitude-dependent time scales requires careful scaling of the equations. In §3 we will present a comprehensive wave–mean interaction theory aimed to be applicable both in the early stage of evolution (in which the vortices build up and bottom friction is negligible) and in the later stage (in which they advect nonlinearly and are affected by bottom friction). This will be achieved by explicit re-scaling of the equations at an appropriate transition time between the two stages.

In §4 we present idealized nonlinear numerical simulations of the entire wave–vortex dynamics using the shallow-water equations with bottom topography and bottom friction. In these equations wave breaking occurs through shock formation, and the advantage is that this requires no adjustable diffusion parameters. The simulations broadly confirm our theoretical predictions, in particular they demonstrate the marked current dislocation effect in the case of inhomogeneous wavetrains incident on barred beaches. They also allow us to see the detailed effect of nonlinear bottom friction, which is hard to understand theoretically.

Concluding remarks are given in §5. In particular, we briefly discuss there the major assumption that has to be made throughout in this paper, namely that a picture based essentially on a single wavetrain (or on several well separated wavetrains) can give useful results for real surf zones. This is important, because real breaking waves are usually not well separated in the alongshore direction. Despite its marginal validity, this assumption has been made here because it allows us to make substantial analytical progress and to bring out the fluid-dynamical mechanisms most clearly, and at affordable numerical cost. Going beyond this assumption is a possible direction for further research.

2. Vortex dynamics on sloping beaches

We present a simple theory for the motion of two-dimensional vortices on a sloping beach. For clarity, the frictionless motion of a single vortex couple is considered first, followed by an account of how nonlinear bottom friction and the presence of other vortex couples might affect the dynamics. Gravity waves are absent here; their rôle will be examined in §3.

2.1. *Single vortex couple*

Consider the dipolar vorticity structure in figure 1(*b*). We can imagine this structure to have been generated by the breaking of a single, transient packet of gravity waves somewhere in the surf zone. This allows us to ignore the gravity waves as far as their impact on the subsequent vortex dynamics is concerned. We idealize the dipolar structure as a vortex couple consisting of two circular vortices with oppositely signed circulations. (For simplicity, we suppress here the small inclination of the vortex couple that is due to the oblique incidence of the original wave packet.) The vortex dynamics itself is a shallow low-Froude-number flow, i.e. the typical flow speed is small compared to the gravity-wave speed. A reasonable first approximation for the vortex dynamics is then to neglect surface undulations altogether by demanding that the layer depth $h = h_S$ everywhere (cf. figure 2). This leads to the shallow-water equations with a rigid upper lid (also called the zero-Froude-number limit of the shallow-water equations). These are the continuity equation

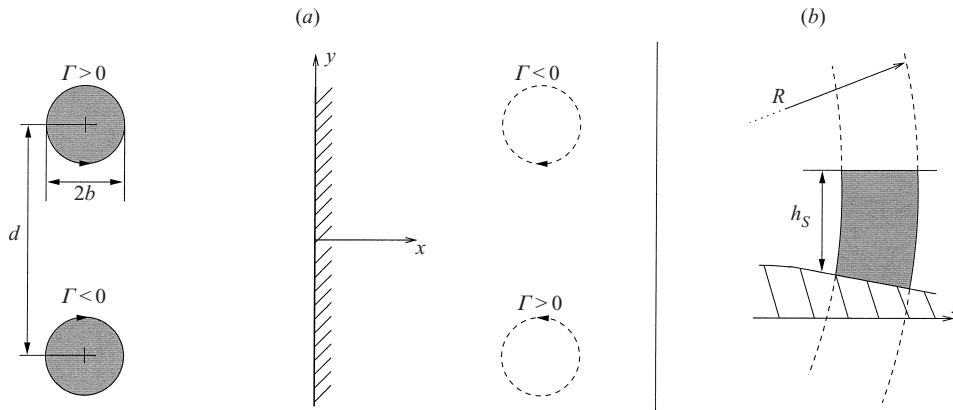$$\nabla \cdot (h_S \boldsymbol{u}) = 0, \tag{2.1}$$

FIGURE 3. (*a*) Idealized vortex couple generated by localized wave breaking in the surf zone. The vortices have equal radius *b*, equal and opposite circulations Γ, and are separated by a distance *d*. The radius *b* is assumed small compared to *d*, to the distance from the shoreline, and to the gradient length scale of the topography $1/|\nabla h_S|$. Also shown in dashed outline are the approximate image vortices obtained by reflecting the vortices at the shoreline. (*b*) Cross-section through one vortex just shorewards of a bar crest. This shows the vortex tube curvature induced by the sloping topography. Also shown is the virtual extension of the vortex tube to a three-dimensional vortex ring with radius *R*. See text for details.

and the horizontal momentum equation

$$\frac{\mathrm{D}\boldsymbol{u}}{\mathrm{D}t} + \frac{1}{\rho}\nabla p = 0. \tag{2.2}$$

Here h_S is the given (and constant in time) still water depth, $\boldsymbol{u} = (u, v)$ is the two-dimensional velocity in the (x, y) directions, ρ is the uniform water density, and p is the pressure at the upper surface, i.e. at the rigid lid. Note that in the case of uniform h_S these equations reduce to the usual two-dimensional incompressible fluid equations. The velocity boundary conditions are decay to zero as $x^2 + y^2 \to \infty$ and $u = 0$ at the shoreline $x = 0$.

The flow described by these equations satisfies Kelvin's circulation theorem and this in turn implies the material conservation of potential vorticity (PV) in the form

$$q \equiv \frac{\nabla \times \boldsymbol{u}}{h_S}, \quad \frac{\mathrm{D}q}{\mathrm{D}t} = 0, \tag{2.3}$$

where $\nabla \times \boldsymbol{u}$ is treated as a pseudoscalar. This highlights that the vorticity following a material fluid column changes due to the stretching or squeezing of the column as it travels over the sloping topography (e.g. Peregrine 1998). In particular, the vorticity strength increases if the column moves into deeper water, and vice versa. By mass conservation, the volume of the column remains constant and this implies that its (x, y) cross-sectional area is proportional to $1/h_S$. Stokes's theorem then ensures that the circulation Γ around the column remains constant, as it has to be.

The motion of the vortex couple is due to two distinct effects: the mutual advection of the vortices (taking due account of the boundary condition at the shoreline), and the self-advection due to sloping topography. In principle, the motion can be calculated exactly by solving a complicated PV-inversion problem in which the velocity field $\boldsymbol{u}$ is calculated from the PV field q under the constraint (2.1) (cf. Richardson 2000). However, in order to gain a robust qualitative understanding of the vortex dynamics,

we will proceed here by modelling the motion with a few simple approximations, as follows.

Consider figure 3(*a*). Due to the conserved circulation Γ even in the presence of sloping topography, the azimuthal velocity around a vortex must still decay as $\Gamma/(2\pi r)$ in the far field (where r is the distance from the vortex), although this velocity will in general depend also on the azimuthal angle. Still, this suggests that the mutual advection should be approximately the same as that which occurs in standard point-vortex dynamics, at least if the two vortices are located roughly in the same topography region. This means that there is an approximate advection of the couple towards the shoreline with velocity $\Gamma/(2\pi d)$. At the same time, the no-normal-flow condition at the shoreline can be accounted for by introducing an appropriate image vortex couple. As is well-known, the resultant flow is an approach to the shoreline by the couple, followed by a separation of the vortices in the alongshore directions, the vortex with $\Gamma > 0$ moving towards increasing y, and vice versa (e.g. Lamb 1932, §155.3).

To this motion must be added the self-advection of the vortices due to the sloping topography, which induces a curvature of the three-dimensional vortex lines as shown in figure 3(*b*). A heuristic approximation of this effect is well-known in coastal oceanography (e.g. Peregrine 1998; Thorpe & Centurioni 2000). In it the self-advection of the vortex is approximated by the self-advection of a three-dimensional vortex ring that results from extending the tube into a three-dimensional virtual vortex ring with radius R. This approximation is based on the similarity between (2.1), which can be solved by introducing a stream function for the mass flow, and the three-dimensional continuity equation for axisymmetric flow, which can be solved by using Stokes's stream function (e.g. Lamb 1932, §94). If one can assume that locally $h_S \propto R$, with R measured from a suitable origin, then this similarity gives a simple approximation for the flow induced by the local topography slope. The radius R is

$$R = h_S/|\nabla h_S|, \tag{2.4}$$

which is the distance over which the water depth would be reduced to zero if it had uniform slope equal to the local slope. Note that on a planar beach R is the distance to the shoreline, in which special case the vortex ring approximation yields exact results (e.g. Thorpe & Centurioni 2000).

Now, the speed of propagation of thin, circular vortex rings with core radius b and ring radius R is (cf. Lamb 1932, §163)

$$\text{vortex speed} = \frac{\Gamma}{4\pi R}\left(\ln\left(\frac{8R}{b}\right) - \frac{1}{4}\right), \tag{2.5}$$

which is valid for $b \ll R$. This is therefore the approximate self-advection speed of the vortices on a sloping beach. The direction of propagation is along isolines of h_S, with a sense of direction such that a vortex with $\Gamma > 0$ in figure 3(*b*) would propagate out of the picture. As is clear from (2.5), the self-advection speed increases with decreasing vortex radius b, although this dependence is logarithmic and hence quite weak. Due to mass conservation of the vortex we have $b^2 h_S =$ const., or

$$b = b_0(h_{S0}/h_S)^{1/2} \tag{2.6}$$

if one introduces the 'potential radius' b_0 that the vortex would have if it were in water of some reference depth h_{S0}. Putting (2.4)–(2.6) together then gives the following

expression for the self-advection velocity U:

$$U = \frac{\Gamma}{4\pi} \left(\frac{\nabla h_S}{h_S} \times \hat{z} \right) \left(\ln \left(\frac{8}{b_0 h_{S0}^{1/2}} \frac{h_S^{3/2}}{|\nabla h_S|} \right) - \frac{1}{4} \right), \tag{2.7}$$

where $\hat{z}$ is the unit vector normal to the (x, y)-plane. It is attractive to see explicitly the dependence of the logarithmic term on h_S, but one should keep in mind that changes in U as the vortex travels are likely to be dominated by changes in the term $\nabla h_S / h_S$ in the cross-product.

What can now be inferred about the qualitative motion of the vortex couple? The sign of U depends on the sign of Γ and hence, as can be readily verified from (2.7), the effect of the self-advection is to reduce the vortex separation d if the couple moves into deeper water, whilst it increases d if the couple moves into shallower water. This in turn implies that the mutual advection (which is proportional to $1/d$) intensifies if the couple moves into deeper water, and vice versa in the other case. The approaching shoreline adds a tendency of increasing separation d due to the image couple. These conclusions can be drawn quite generally, and it is not difficult to add quantitative detail for a specific profile $h_S(x)$.

The net result is that in the case of a planar beach the vortices will be separated quickly due to a constructive superposition of the separating tendencies due to self-advection and to the approaching shoreline. One can hence hypothesize that the vortex couple will not make much headway up a planar beach before the vortices effectively are completely separated. This is in good qualitative agreement with the numerical vortex couple simulations presented in Richardson (2000). In contrast, in the case of a barred beach the couple first moves into the deeper water of the bar trough, which brings the vortices closer together due to the self-advection (at least if the shoreline is sufficiently far away). This means that the couple speeds up, and makes good progress until it has to climb the other side of the trough. Then the same process as on the planar beach sets in, leading to rapid separation of the vortices in the alongshore direction. This leads to the hypothesis that vortices will easily move into the bar trough, but will not make much headway climbing out of it again. The overall prediction is therefore that vortex couples produced by breaking waves on the bar crest will in all likelihood later be found in or close to the bar trough.

In this way the region of fast-moving fluid between the vortices is moved away from the breaking region and into the bar trough. If one now allows an inclined vortex couple to represent the breaking of oblique waves, one can begin to see a picture of the longshore current as being composed of these fast-moving regions between vortices. The average current location can then be identified with the likely long-time location of the vortices, which hence explains why the longshore current can be found in the bar trough even though the wave breaking may be concentrated on the bar crest. The vortex dynamics described here hence offers a possible explanation of the current dislocation observed on barred beaches.

As an aside, note that on a planar beach these considerations imply that in a seaward-moving couple, i.e. a couple moving *away* from the shoreline, the vortices will move closer together due to the self-advection. Hence, the couple will speed up due to the intensified mutual advection. The region of fast-moving fluid between the vortices will also get narrower and quicker, which is a vivid manifestation of the well-known 'rip currents', which can carry a swimmer hundreds of metres offshore. Peregrine (1998, §3.2), however, argues that a seaward-moving couple should slow down rather than speed up. Presumably, such slowing-down behaviour would have to

be caused by frictional or three-dimensional effects that are neglected here. Eventually, deep-water three-dimensional instabilities must set in, which presumably will destroy most of the coherent vortex couple and hence stop the rip current.

2.2. *Bottom friction*

The fluid experiences a viscous boundary layer drag at the bottom, which is usually modelled by a turbulent friction term in the momentum equation (e.g. LH70a, b). The momentum equation (2.2) then becomes

$$\frac{\mathrm{D}\boldsymbol{u}}{\mathrm{D}t} + \frac{1}{\rho}\nabla p = -\frac{c_f}{h_S}|\boldsymbol{u}|\boldsymbol{u}, \tag{2.8}$$

where the empirically determined non-dimensional friction coefficient $c_f \approx 0.01$. The friction term allows momentum to be transferred from the fluid into the ground, and its form ensures that kinetic energy is always diminished. The fact that the friction term is quadratic in the velocity means that it scales with flow speed in the same way as the term $(\boldsymbol{u}\cdot\nabla)\boldsymbol{u}$ in the material derivative. This means that the relative importance of the friction term for the advective vortex dynamics is governed purely by c_f/h_S. For instance, the ratio of advective to frictional time scales is the same for vortices of the same geometry but different amplitude. This means that strong and weak vortices travel the same distance before their energy has been dissipated, the only difference being that the stronger vortex will reach this distance more quickly. (Another way to see this is to note that (2.8) and (2.1) are symmetric under the transformation $\boldsymbol{u} \to \alpha\boldsymbol{u}$, $p \to \alpha^2 p$, and $t \to \alpha^{-1}t$ for $\alpha > 0$. See § 3.5 for further discussion of this symmetry.) We note that, as the friction strength is inversely proportional to h_S, it seems that a bar trough is a location of comparatively weak bottom friction, though the implications of this for vortical structures are not clear.

It would certainly be convenient if one could assume that for $c_f \ll 1$ the friction simply attenuates the vortex couple dynamics over a time scale long compared to a vortex turnover time. However, this does not seem to be the case, as can be seen, for instance, from the PV equation

$$\frac{\mathrm{D}q}{\mathrm{D}t} = -\frac{c_f}{h_S}\nabla \times \left(\frac{|\boldsymbol{u}|\boldsymbol{u}}{h_S}\right). \tag{2.9}$$

In general, the right-hand side will not be zero for irrotational flow even if h_S is uniform. For instance, the azimuthal velocity field $v(r,t)$ and PV $q(r,t)$ of a single axisymmetric vortex on flat terrain (at a fixed radius from the vortex centre $r > 0$) would decay as

$$v(r,t) = \frac{v(r,0)}{1 + (t\,v(r,0)c_f/h_S)} \approx \frac{h_S}{tc_f}, \quad q \approx \frac{h_S}{r\,tc_f} \quad \text{as} \quad t \to \infty. \tag{2.10}$$

Clearly, q does not exhibit any simple behaviour, i.e. it becomes non-zero in regions of initially potential flow, and it becomes non-uniform in regions that were initially in solid-body rotation. This means that one cannot rigorously speak of isolated vortices any more once frictional effects have become noticeable. Therefore, one has to anticipate the possibility that the simplistic picture of the flow dynamics in terms of the motion of a single vortex couple breaks down on a frictional time scale. The study of such flows can still be pursued numerically (as in § 4), but to our knowledge a theoretical description of this regime has not been given and remains open for future research.

Therefore, it seems prudent here to hypothesize no further than to remark simply that the energy dissipation due to bottom friction must eventually diminish the

capacity for coherent propagation of the vortex couple, and that the concomitant loss of coherence of the couple also hinders its further propagation. Coherent propagation over a finite distance is still possible provided that the advective time scale is shorter than the friction time scale, i.e. provided that the friction coefficient c_f is small enough.

As an aside, we note that in the less relevant case of linear bottom friction (i.e. Rayleigh damping) the vortices would remain coherent whilst decaying exponentially (for uniform h_S). In that case stronger vortices would also travel larger distances than weaker vortices before succumbing to dissipative decay; the travel distance would be proportional to the vortex amplitude.

2.3. *Motion of several vortex couples*

The above results for a single couple can be used to arrive at some useful conclusions for the motion of several vortex couples that are forced, say, by an array of wavetrains staggered in the y-direction. Each wavetrain forces a couple that behaves roughly as described above, at least if the wavetrains are well separated. As stated before (leaving aside frictional effects), the vortices in a couple will eventually separate in the alongshore direction, with the $\Gamma > 0$ vortex moving towards increasing y and vice versa. What happens next depends on the strength of the bottom friction: if c_f is small enough, then the $\Gamma > 0$ vortex might meet the $\Gamma < 0$ vortex produced by the adjacent wavetrain, which travels in the opposite direction. These vortices can now form a new couple moving seawards. On a planar beach this new couple would be recognized as a rip current. On a barred beach the couple might separate again when it tries to climb the bar crest in a seaward direction. Then one could imagine a further sequence of encounters with oppositely signed vortices emanating from adjacent wavetrains, leading to a complicated meandering motion of the vortices across the bar trough, with eventual decay due to bottom friction. It might be possible that this decay is least pronounced in the bar trough (because of the factor $1/h_S$ in (2.8)), which adds another attractive feature to this location.

These scenarios neglect the loss of coherence due to nonlinear bottom friction and due to the stripping apart of vortex filaments that must come into play once sufficiently many vortices are present to make the ideas of two-dimensional turbulence theory applicable. Nevertheless, it is interesting to note that in the envisaged dynamics the bar trough appears to be capable of trapping the vortices and thereby of attracting the longshore current into this preferred location.

3. Wave–mean interaction theory

The wave–mean interaction theory for the surf zone is formulated here in a shallow-water model. The theory is based on an asymptotic expansion in wave amplitude, which hence has to be small. No detailed wave shape is assumed, but specific results based on ray tracing for sinusoidal waves are noted. By combining the radiation-stress theory of LH70*a* with the results from B2000, a theory valid for an inhomogeneous wavetrain is formulated. Careful scaling has to be undertaken in order to capture both the early stage of mean-flow vorticity growth, and the later stage of mean-flow vortex advection and vortex decay due to bottom friction. This also yields explicit scaling laws for the mean-flow response.

3.1. *Shallow-water model*

We use a free-surface shallow-water model with variable bottom topography as the simplest possible model for the surf zone. The main advantages are that both

waves and vortices can be described by the same mathematical model, and that their interaction theory can be developed fully and explicitly and without restriction, say, to irrotational flow. The main disadvantage is that shallow-water waves poorly approximate deep ocean waves, e.g. the non-dispersive shallow-water waves form shocks even over flat topography, which is not the case for deep ocean waves.

The governing equations are the continuity equation

$$\frac{\partial h}{\partial t} + \nabla \cdot (h\boldsymbol{u}) = 0 \tag{3.1}$$

for the layer depth $h(x, y, t)$ and the momentum equation

$$\frac{D\boldsymbol{u}}{Dt} + g\nabla(h + h_B) = \boldsymbol{F} - \frac{c_f}{h}|\boldsymbol{u}|\boldsymbol{u} \tag{3.2}$$

for the velocity $\boldsymbol{u}(x, y, t) = (u, v)$. Here g is gravity, h_B is the bottom elevation (cf. figure 2), $\boldsymbol{F}$ is an unspecified dissipative body force, and the final term represents the nonlinear bottom friction, as before. We assume that the dissipative force $\boldsymbol{F}$ is scale-selective in a way that makes it negligible in smooth parts of the flow whilst becoming significant when the waves are steepening. In essence, $\boldsymbol{F}$ is a simplistic representation of the dissipation due to shock formation of the shallow-water waves (cf. B2000).†

The full PV is now

$$q = \frac{\nabla \times \boldsymbol{u}}{h}, \quad \text{such that} \quad \frac{Dq}{Dt} = \frac{\nabla \times \boldsymbol{F}}{h} - \frac{c_f}{h}\nabla \times \left(\frac{|\boldsymbol{u}|\boldsymbol{u}}{h}\right). \tag{3.3}$$

We assume that all flow fields ϕ can be split into a mean part $\bar{\phi}$ and a disturbance part ϕ' such that $\phi = \bar{\phi} + \phi'$. The mean part is defined by phase averaging, i.e. by a spatial average of the flow field over a typical wavelength of the waves. (A temporal average over a wave period would give the same results here.) We assume throughout that $\overline{\phi'} = 0$ holds with negligible error, which is certainly justified in the numerical simulations presented in §4. We also assume that all mean variables (e.g. the wavetrain envelope, bottom topography, longshore current velocities) are slowly varying in the horizontal, i.e. that the typical length scale of a mean field is large compared to a typical wavelength of the incoming waves. Formally, if the gradients of disturbance fields are $O(1)$, then the gradients of mean fields are $O(\mu)$, where $\mu \ll 1$ is a suitable small parameter measuring the scale separation.

We are looking for the mean-flow response to slowly varying small-amplitude gravity waves propagating on a background state of rest. Formally, we introduce a non-dimensional wave amplitude $a \ll 1$ such that the background state is $O(1)$, the waves are $O(a)$, and the mean-flow response is $O(a^2)$. We will treat this problem first by a regular perturbation expansion in a, which is valid up to times $t = O(1)$. (As an aside (cf. B2000), we note that an expansion valid for $t = O(1)$ cannot describe the self-induced shock formation of small-amplitude gravity waves, which occurs over a time scale $t = O(a^{-1})$.) This expansion allows us to derive detailed results for the early stages of the mean-flow evolution with minimal technical effort. The later stage

† In the analogy with two-dimensional flow of a homentropic perfect gas with ratio of specific heats equal to 2, the gas density would correspond to h, and h_B would correspond to an external field potential that leads to an inhomogeneous background density h_S such that $h_S + h_B = \text{const.}$ Small-amplitude wave dissipation in gas dynamics upsets homentropy only by a small amount of third order in wave amplitude, and hence we note that our asymptotic results are applicable to nonlinear acoustics and sound–vortex interactions.

of the mean-flow evolution at times up to $t = O(a^{-1})$ is described separately in §3.5, where the saturation of the mean-flow amplitude at $O(a)$ is discussed.

3.2. *Linear waves*

We now turn to the perturbation expansion in wave amplitude a. The $O(1)$ background state has zero velocity and a flat surface. This means that the background layer depth is equal to $h_S(x) = h_{S0} - h_B(x)$, where h_{S0} is a constant reference depth at a suitable seaward location where $h_B = 0$. The local wave speed is then

$$c(x) = \sqrt{gh_S(x)}. \tag{3.4}$$

A suitable definition for the non-dimensional wave amplitude is $a = \max(h'/h_S)$, where the maximum is taken over a wavelength. For plane monochromatic waves this is equivalent to $a = \max(|\boldsymbol{u}'|/c)$. To find the governing equations for the linear gravity waves we set $\boldsymbol{u} = \boldsymbol{u}' + O(a^2)$ and $h = h_S + h' + O(a^2)$ and collect terms at $O(a)$ in (3.1)–(3.2). This gives

$$\frac{\partial h'}{\partial t} + \nabla \cdot (h_S \boldsymbol{u}') = 0, \tag{3.5}$$

$$\frac{\partial \boldsymbol{u}'}{\partial t} + g\nabla h' = \boldsymbol{F}'. \tag{3.6}$$

Note that bottom friction does not enter at $O(a)$. Indeed, it will turn out that the bottom friction can also be neglected at $O(a^2)$ in the early stage of the evolution, i.e. friction only becomes important at the later stage described in §3.5. The equations (3.5)–(3.6) with $\boldsymbol{F}' = 0$ admit the usual irrotational non-dispersive gravity waves subject to refraction caused by the slowly varying layer depth $h_S(x)$. For $\boldsymbol{F}' \neq 0$ these waves are damped and there can also be a vorticity part due to

$$\frac{\partial(\nabla \times \boldsymbol{u}')}{\partial t} = \nabla \times \boldsymbol{F}'. \tag{3.7}$$

The theory developed here does not depend on $\nabla \times \boldsymbol{u}' = 0$, even though $\nabla \times \boldsymbol{F}'$ is often negligible at $O(a)$.

It is convenient to introduce linear particle displacements $\boldsymbol{\xi}' = (\xi', \eta')$ by

$$\frac{\partial \boldsymbol{\xi}'}{\partial t} = \boldsymbol{u}', \quad \text{such that} \quad h' + \nabla \cdot (h_S \boldsymbol{\xi}') = 0 \tag{3.8}$$

can be obtained by integrating (3.5) in time. We now calculate several $O(a^2)$ wave properties, which are averaged squares of the $O(a)$ solutions and hence depend only on the linearized equations. These wave properties will enter the equations for the mean-flow response. The wave energy per unit mass† is defined as

$$E = \frac{1}{2}\left(\overline{u'^2} + \overline{v'^2} + g\frac{\overline{h'^2}}{h_S}\right) \tag{3.9}$$

and using (3.5)–(3.6) it can easily be shown to satisfy

$$\frac{\partial E}{\partial t} + \frac{1}{h_S}\nabla \cdot (gh_S\,\overline{h'\boldsymbol{u}'}) = \overline{\boldsymbol{u}' \cdot \boldsymbol{F}'}, \tag{3.10}$$

which shows that the area integral of $h_S E$ is conserved in the absence of $\boldsymbol{F}'$, as is

---

† We use energy per unit mass partly to aid the analogy with nonlinear acoustics. Water wave studies often use the energy per unit area, which is $h_S E$ here.

to be expected for waves on a background state of rest. It can be seen that, strictly speaking, the dissipative force should satisfy $F' \leqslant O(\mu a)$ in order to be consistent with the assumption of a slowly varying wavetrain envelope.

Another useful wave property is the so-called Stokes drift $\bar{u}^S$, which is defined as the difference between the Lagrangian (i.e. particle-following) mean velocity $\bar{u}^L$ and the Eulerian mean velocity $\bar{u}$. Its general functional expression is complicated but to $O(a^2)$ it is given by (cf. Andrews & McIntyre 1978)

$$\bar{u}^S = \overline{(\xi' \cdot \nabla) u'} = \frac{1}{h_S} \overline{(h_S \xi' \cdot \nabla) u'} = -\frac{1}{h_S} \overline{\nabla \cdot (h_S \xi') u'} + O(\mu a^2) \approx +\frac{1}{h_S} \overline{h' u'}, \qquad (3.11)$$

after using (3.8) and neglecting the envelope term $O(\mu a^2)$. Analogous expressions hold for all Stokes corrections $\bar{\phi}^S = \bar{\phi}^L - \bar{\phi}$.

Of particular importance is the so-called pseudomomentum per unit mass p, which occurs naturally in wave–mean interaction theory, especially when considering averaged versions of the circulation theorem, or of the PV definition in (3.3) (cf. B2000). Its components are given to $O(a^2)$ by

$$p_i = -\overline{\xi'_{j,i} u'_j} = +\overline{\xi'_j u'_{j,i}} + O(\mu a^2) \approx \overline{\xi'_j u'_{i,j}} + \overline{\xi'_j (u'_{j,i} - u'_{i,j})}, \qquad (3.12)$$

$$p = \bar{u}^S + \overline{\xi' \times \hat{z}(\nabla \times u')} = \frac{1}{h_S} \overline{h' u'} + \overline{\xi' \times \hat{z}(\nabla \times u')}, \qquad (3.13)$$

where commas denote differentiation and the summation convention has been used. The evolution equation for p is obtained by multiplying (3.6) with h'/h_S, averaging, and some further manipulations, which are detailed in an Appendix. The result is

$$\frac{\partial p_i}{\partial t} + \frac{1}{h_S} \frac{\partial}{\partial x_j} \left(h_S \overline{u'_i u'_j} + \delta_{ij} \frac{h_S}{2} \left[g \overline{\frac{h'^2}{h_S}} - \overline{|u'|^2} \right] \right) + \frac{\overline{|u'|^2}}{2h_S} \frac{\partial h_S}{\partial x_i} = -\overline{\xi'_{j,i} F'_j} \equiv \mathscr{F}_i, \qquad (3.14)$$

where the dissipative force $\mathscr{F}$ captures the dissipative decay of p. It will turn out that $\mathscr{F}$ is central to the mean-flow vorticity forcing. (To get a feel for the way $\mathscr{F}$ affects the waves one can consider the generic case $\mathscr{F} = -\tau^{-1} p$ for some dissipative time scale τ.) We note that if h_S depends only on x, then in the absence of dissipation the y-component of the area integral of $h_S p$ is conserved. However, the x-component of pseudomomentum is not conserved. Specifically, x-pseudomomentum is generated wherever the slope of h_S is negative and vice versa. For instance, the total x-pseudomomentum contained in a wavepacket climbing a planar beach is increased (cf. B2000).

For completeness we briefly summarize now some useful expressions for the linear waves based on ray tracing for a slowly varying wavetrain containing sinusoidal waves. The attraction of ray theory is that it gives physically plausible results with very little effort, for instance the ray-tracing expressions will be valid for general $h_S(x, y)$. At the very least, these results can then be used as guide for understanding the real phenomena.

For simplicity, we consider a steady wavetrain with uniform frequency. Locally, the gradient of the wave phase is given by a slowly varying wavenumber vector field $k = (k, l)$ that satisfies the integrability condition $\nabla \times k = 0$. The time derivative of the phase is given by minus the frequency ω subject to the dispersion relation $\omega = c\kappa$, where the depth-dependent wave speed $c = \sqrt{g h_S}$ and $\kappa = |k|$. The $O(1)$ background state is steady, and due to the assumption of uniform frequency we have

$$\omega = \omega_0 = \sqrt{g h_{S0}} \kappa_0 \quad \text{everywhere, which implies} \quad h_S \kappa^2 = h_{S0} \kappa_0^2 \qquad (3.15)$$

using the reference depth h_{S0} at a suitable seaward location. This implies that $\kappa > \kappa_0$ as the water depth decreases. As is readily verified from the linear plane wave solutions, the local wave structure has $\boldsymbol{u}'$ parallel to $\boldsymbol{k}$, group velocity $\boldsymbol{c}^g = c\boldsymbol{k}/\kappa$, and satisfies energy equipartition such that

$$E = \overline{|\boldsymbol{u}'|^2} = g\overline{h'^2}/h_S = gh_S\, a^2/2, \tag{3.16}$$

where a is the non-dimensional wave amplitude. The Stokes drift and pseudomomentum are both given by

$$\bar{\boldsymbol{u}}^S = \boldsymbol{p} = \frac{\boldsymbol{k}}{\omega}E. \tag{3.17}$$

Note that in the presence of an $O(1)$ background flow the intrinsic frequency would appear in (3.17). We see that $\boldsymbol{p}$ is independent of the wavelength of the non-dispersive waves considered here, for which $\omega \propto \kappa$.

The rate of change per unit time of $\boldsymbol{k}$ along a group-velocity ray is given by

$$\frac{\partial \boldsymbol{k}}{\partial t} + (\boldsymbol{c}^g \cdot \nabla)\boldsymbol{k} = -\kappa \nabla c,$$

which yields

$$\frac{1}{\kappa^2}(\boldsymbol{k} \cdot \nabla)\boldsymbol{k} = -\frac{1}{2h_S}\nabla h_S. \tag{3.18}$$

Clearly, if h_S is independent of y then $l = $ const. along rays.

Combining (3.10), (3.14) and (3.17), we see that in fact $\mathscr{F} = \boldsymbol{k}\omega^{-1}\,\overline{\boldsymbol{u}' \cdot \boldsymbol{F}'}$, which can also be seen directly from $k_i\omega^{-1}u'_j = \xi'_{j,i}$. Therefore, multiplying (3.10) by $\boldsymbol{k}\omega^{-1}$ and using (3.11), (3.15) and (3.17) gives

$$\boxed{\mathscr{F} = \frac{\boldsymbol{k}}{h_S}\nabla \cdot \left(h_S\frac{\boldsymbol{k}}{\kappa^2}E\right).} \tag{3.19}$$

The same equation can also be derived from (3.14) and (3.18). This shows that $\mathscr{F}$ is parallel to $-\boldsymbol{k}$ and hence to $-\boldsymbol{p}$, as expected.

Equation (3.19) is valid for general $h_S(x, y)$ and $\boldsymbol{k}(x, y)$, at least in the absence of caustics due to intersecting rays. We will now simplify (3.19) by assuming (i) that $h_S = h_S(x)$, (ii) that the angle of incidence is small (i.e. $|l_0| \ll \kappa_0$), and (iii) that all rays orginate from a seaward reference location $x = x_0$ with uniform $\boldsymbol{k}(x_0, y) = (k_0, l_0)$, where $k_0 > 0$ and l_0 are constants. The wave amplitude at $x = x_0$ is still allowed to vary with y. Together, (i) and (iii) imply that $l = l_0$ everywhere, and (ii) allows the use of the small-angle approximation, in which only terms $O(l_0/\kappa_0)$ are retained. Also, (iii) implies that parallel rays emerge from $x = x_0$ and hence focusing effects in y are absent. Using $l = l_0$ and (3.15), the wavenumber $k > 0$ is given by

$$k(x) = \kappa\sqrt{1 - \frac{l_0^2}{\kappa^2}} \approx \kappa = \kappa_0\sqrt{\frac{h_{S0}}{h_S(x)}}, \tag{3.20}$$

in the small-angle approximation. Now, $\nabla \cdot (\boldsymbol{k}\kappa^{-1}) \approx 0$ in the same approximation, and this can be used to simplify (3.19) to

$$\mathscr{F} = \frac{\boldsymbol{k}}{h_S}\left\{\frac{1}{\kappa}(\boldsymbol{k} \cdot \nabla)\left(\frac{h_S E}{\kappa}\right) + \left(\frac{h_S E}{\kappa}\right)\nabla \cdot \left(\frac{\boldsymbol{k}}{\kappa}\right)\right\} \approx \frac{\boldsymbol{k}}{h_S\kappa}(\boldsymbol{k} \cdot \nabla)\left(\frac{h_S E}{\kappa}\right). \tag{3.21}$$

Using (3.15) again, we see that $h_S^{3/2}E$ is constant along rays in the absence of

dissipation. By (3.16) this implies that $a \propto h_S^{-5/4}$ in this case, which quantifies the amplitude growth of the waves. Using (3.20) and (3.15) the components of $\mathscr{F}$ can be given explicitly as

$$\mathscr{F}_x = \frac{1}{h_S^{3/2}} \frac{\partial}{\partial x}(h_S^{3/2}E) + \sqrt{\frac{h_S}{h_{S0}}} \frac{l_0}{\kappa_0} \frac{\partial E}{\partial y}, \quad \mathscr{F}_y = \frac{1}{h_S\sqrt{h_{S0}}} \frac{l_0}{\kappa_0} \frac{\partial}{\partial x}(h_S^{3/2}E). \quad (3.22)$$

Following LH70a,b, one could now consider a saturation criterion such that $a = $ const. after the onset of breaking. By (3.16) this means that $E \propto h_S$ and hence $\mathscr{F}$ can in principle be quantified for a given $h_S(x)$, subject to care with complications due to amplitude variations in y and due to the possible switch-off of wave breaking over the bar trough, where a could sink again below the breaking threshold.

3.3. *Mean-flow response: early stage*

We now turn the equations for the mean-flow response. Averaging the continuity equation (3.1) gives

$$\frac{\partial \bar{h}}{\partial t} + \nabla \cdot (\bar{h}\bar{u} + \overline{h'u'}) = 0. \quad (3.23)$$

Introducing the depth set-up $\overline{\Delta h} = O(a^2)$ via $\bar{h} = h_S + \overline{\Delta h}$, noting that $\bar{u} = O(a^2)$ and collecting terms at $O(a^2)$ then gives

$$\boxed{\frac{\partial \overline{\Delta h}}{\partial t} + \nabla \cdot (h_S \bar{u}^L) = 0,} \quad \text{where} \quad \bar{u}^L = \bar{u} + \bar{u}^S. \quad (3.24)$$

Thus the depth set-up changes according to the transport of h_S with the Lagrangian-mean velocity $\bar{u}^L$. A suitable boundary condition at $x = 0$ is $\bar{u}^L = 0$. The mean momentum equation is somewhat more cumbersome to derive and it is perhaps less clear what its optimal form should be. We will manipulate it into a form in which the radiation-stress tensor appears, and then we will consider the relation of that stress tensor to $\mathscr{F}$. Before this, we note the argument given in LH70a,b that shows that the bottom friction term in (3.2) is still negligible at $O(a^2)$, where because of $\bar{u} = O(a^2)$ it equals

$$-\frac{c_f}{h_S} \nabla \times \left(\frac{\overline{|u'|u'}}{h_S} \right). \quad (3.25)$$

Here u' comes from the linear solution and for a plane monochromatic wave the resultant friction force averages to zero. We will assume here that this allows us to neglect the friction term.

Now, averaging (3.2) without the friction term results in

$$\frac{\partial \bar{u}}{\partial t} + (\bar{u} \cdot \nabla)\bar{u} + \overline{(u' \cdot \nabla)u'} + g\nabla(\bar{h} + h_B) = \bar{F}. \quad (3.26)$$

Introducing $\overline{\Delta h}$ as before means that because $h_S + h_B = h_{S0}$ we have $\nabla(\bar{h} + h_B) = \nabla\overline{\Delta h}$, and collecting terms at $O(a^2)$ then gives

$$\frac{\partial \bar{u}}{\partial t} + \overline{(u' \cdot \nabla)u'} + g\nabla\overline{\Delta h} = \bar{F}. \quad (3.27)$$

The second term contains u' from the linear solution, and we can manipulate it as

follows:

$$\overline{(\boldsymbol{u'} \cdot \nabla)\boldsymbol{u'}} = \frac{1}{h_S} \nabla \cdot (h_S \overline{\boldsymbol{u'u'}}) - \frac{1}{h_S} \overline{\nabla \cdot (h_S \boldsymbol{u'})\boldsymbol{u'}} \tag{3.28}$$

$$= \frac{1}{h_S} \nabla \cdot (h_S \overline{\boldsymbol{u'u'}}) + \frac{1}{h_S} \overline{\frac{\partial h'}{\partial t} \boldsymbol{u'}} \tag{3.29}$$

$$= \frac{1}{h_S} \nabla \cdot (h_S \overline{\boldsymbol{u'u'}}) + \frac{\partial \overline{\boldsymbol{u}}^S}{\partial t} - \frac{1}{h_S} \overline{h' \frac{\partial \boldsymbol{u'}}{\partial t}} \tag{3.30}$$

$$= \frac{1}{h_S} \nabla \cdot (h_S \overline{\boldsymbol{u'u'}}) + \frac{\partial \overline{\boldsymbol{u}}^S}{\partial t} - \frac{1}{h_S} \overline{h'\boldsymbol{F'}} + \frac{g}{2h_S} \nabla \overline{h'^2}. \tag{3.31}$$

Substituting back into (3.27) and rearranging then results in

$$\frac{\partial \overline{\boldsymbol{u}}^L}{\partial t} + \frac{1}{h_S} \nabla \cdot \left(h_S \overline{\boldsymbol{u'u'}} + \boldsymbol{\delta} \frac{g}{2} \overline{h'^2} \right) + g\nabla \overline{\Delta h} = \overline{\boldsymbol{F}}^L, \tag{3.32}$$

where $\boldsymbol{\delta}$ is the unit tensor with components δ_{ij}. The quantity in brackets is the radiation-stress tensor $\boldsymbol{S}$ used in LH70*a, b*. Its components are

$$S_{ij} = h_S \overline{u_i' u_j'} + \delta_{ij} \frac{g}{2} \overline{h'^2}. \tag{3.33}$$

The right-hand side of (3.32) still contains an explicit dissipation term equal to $\overline{\boldsymbol{F}}^L$. However, as pointed out in §4 of B2000, in the case of slowly varying mean quantities and a *momentum-conserving* dissipative force (i.e. a force that derives from a stress tensor divergence as $F_i = h^{-1}\sigma_{ij,j}$) it turns out that $|\overline{F}_i^L| \ll |\mathscr{F}_i|$, by a factor of $O(\mu)$. By taking the scale for $|\mathscr{F}_i|$ from (3.14) we see that $\overline{\boldsymbol{F}}^L$ is in fact negligible in (3.32). We stress again that this does not hold for arbitrary forces $\boldsymbol{F}$, but only for momentum-conserving forces such as those arising in the Navier–Stokes equations. For instance, $\overline{\boldsymbol{F}}^L$ would not be negligible in the case of Rayleigh damping, where $\boldsymbol{F} \propto -\boldsymbol{u}$ and hence $\overline{\boldsymbol{F}}^L \propto -\overline{\boldsymbol{u}}^L$.

Restricting our considerations now to momentum-conserving forces, we finally obtain

$$\boxed{\frac{\partial \overline{\boldsymbol{u}}^L}{\partial t} + g\nabla \overline{\Delta h} = -\frac{1}{h_S} \nabla \cdot \boldsymbol{S} + \overline{\boldsymbol{F}}^L = -\frac{1}{h_S} \nabla \cdot \boldsymbol{S}} \tag{3.34}$$

to leading order. This equation together with (3.24) completely describes the mean-flow response to the waves because the symmetric tensor $\boldsymbol{S}$ is a wave property and hence depends only on the linear solution.

3.4. *Radiation-stress tensor versus effective dissipative force*

The last section demonstrated that if $\{\overline{\boldsymbol{u}}^L, \overline{\Delta h}\}$ are used as variables then the convergence of the radiation-stress tensor $\boldsymbol{S}$ represents the entire wave-induced forcing of the mean flow (in general, this cannot be achieved in more complicated fluid models, cf., for instance, the discussion of Coriolis forces in §8 in Andrews & McIntyre 1978.) However, the mean flow responds to a number of different physical effects such as wave transience, dissipation, and wave-induced changes in the mean pressure. All these effects combine to make up $\boldsymbol{S}$ and this makes it hard to disentangle, for instance, the dissipative effects that alone can produce vortices because of Kelvin's circulation theorem.

This is not a problem in the case of the steady homogeneous wavetrain treated

in LH70*a*, *b*. There, the *y*-derivatives of all mean fields are zero, and hence the *y*-component of (3.34) simplifies to

$$\frac{\partial \bar{v}^L}{\partial t} = \frac{\partial \bar{v}}{\partial t} + \frac{\partial \bar{v}^S}{\partial t} = \frac{\partial \bar{v}}{\partial t} = -\frac{1}{h_S}\frac{\partial S_{yx}}{\partial x}. \tag{3.35}$$

LH70*a*, *b* demonstrated that the right-hand side of (3.35) is precisely due to wave dissipation and this forms the basis of the successful theory for longshore currents in this case.

However, in the case of a steady but inhomogeneous wavetrain there is now an extra term $-g\partial\overline{\Delta h}/\partial y$ on the left-hand side of (3.35), which complicates the problem. Moreover, the divergence of **S** is then due to other effects in addition to dissipation. Finally, for unsteady wave fields the use of Lagrangian-mean velocities can be avoided no longer, and in addition **S** then contains further terms to do with wave transience.

For this reason it is convenient to decompose the convergence of **S** into parts explicitly linked to the different physical effects. (This mirrors manipulations familiar from the wave–mean interaction theory of atmospheric flows (e.g. Andrews, Holton, & Leovy 1985). However, in these cases the mean flow is usually taken to be axisymmetric.) Specifically, comparing (3.33) and (3.14) we can see that

$$\boxed{-\frac{1}{h_S}\nabla \cdot \boldsymbol{S} = \frac{\partial \boldsymbol{p}}{\partial t} - \mathscr{F} - \tfrac{1}{2}\nabla\overline{|\boldsymbol{u}'|^2}} \tag{3.36}$$

holds, which neatly separates effects due to transience, dissipation, and mean pressure changes. For instance, in the case of steady non-dissipative waves the only non-zero term is the last one, which can then be balanced in (3.34) by a layer depth change $\overline{\Delta h} = -0.5\,\overline{|\boldsymbol{u}'|^2}$ without further mean-flow acceleration. This is a form of the familiar density dilatation effect in acoustics (see Bühler & McIntyre 1998 for a detailed discussion of this effect in rotating shallow water). Also, for a steady homogeneous wavetrain the right-hand side of (3.35) is equal to $-\mathscr{F}\cdot\hat{\boldsymbol{y}}$, which was the case treated in LH70*a*, *b*.

Substituting (3.36) back into (3.34) and taking the curl results in

$$\frac{\partial}{\partial t}\nabla \times (\bar{\boldsymbol{u}}^L - \boldsymbol{p}) = \nabla \times (-\mathscr{F}) \tag{3.37}$$

because the irrotational gradient terms make no contribution. This is in fact the $O(a^2)$ version of a finite-amplitude, nonlinear result derivable using generalized Lagrangian-mean theory (§ 3 in B2000). That theory also shows that, consistent with (3.37), the surprisingly simple relation

$$\bar{q}^L = \left(\frac{\overline{\nabla \times \boldsymbol{u}}}{h}\right)^L = \frac{\nabla \times (\bar{\boldsymbol{u}}^L - \boldsymbol{p})}{h_S} \tag{3.38}$$

holds to $O(a^2)$. Together, (3.37) and (3.38) make obvious the fact that the mean vorticity generation can always be thought of as arising through the action of an effective dissipative force equal to $-\mathscr{F}$. (In the generic case $\mathscr{F} = -\tau^{-1}\boldsymbol{p}$, where τ is a suitable dissipative time scale, this means the effective dissipative force would be equal to $+\tau^{-1}\boldsymbol{p}$, which makes it easy to visualize the effective dissipative force and its curl.)

If the waves are steady then (3.37) simplifies to

$$\frac{\partial}{\partial t}\nabla \times \bar{\boldsymbol{u}} = \nabla \times (-\mathscr{F}) \tag{3.39}$$

because both Stokes drift and pseudomomentum are then constant. This equation retains the simplicity of (3.35) in that there is no coupling to $\overline{\Delta h}$, which neatly separates the vortical mean flow from the rest of the possible mean-flow dynamics (note that the full mean-flow equations (3.24)–(3.34) can support mean-flow gravity waves). Thus, by modelling or measuring the effective dissipative force $-\mathscr{F}$ one can deduce the mean-flow vorticity generation. The modelling could be achieved by the ray-tracing theory described before, whereas measuring $-\mathscr{F}$ in a numerical model can be achieved indirectly by computing the approximate remainder of (3.14) (cf. B2000).

In summary, the net result of the wave–mean interaction theory described so far is that in the early stage of the evolution the mean vorticity grows according to (3.37), or to (3.39) if the wavetrain is steady. The curl of $-\mathscr{F}$ is non-zero because of the envelope structure of the wavetrain, and this leads to the typical dipolar mean vorticity pattern shown previously in figure 1 and figure 3.

3.5. *Mean-flow response: later stage*

So far the focus has been on the early stage of the mean-flow evolution, in which the flow starts from rest and the mean vorticity grows at a rate proportional to $O(a^2)$ in response to the wave dissipation (cf. (3.39)). The asymptotic small-amplitude theory for this early stage is strictly valid only for $t = O(1)$ and hence the generated mean vorticity is never larger than $O(a^2)$, which was seen to imply that bottom friction was negligible. This is quite different from the theory in LH70a,b, in which the early stage was not considered explicitly. Instead, the theory in LH70a,b aimed to solve directly for a final state in which bottom friction and wave forcing balance each other (subject to additional horizontal momentum diffusion). The final longshore mean velocity $\bar{v}$ turned out to be $O(a)$, though it had to be small compared to the $O(a)$ wave velocity $|\boldsymbol{u}'|$ in order for the bottom friction term to take a manageable form.

It is highly desirable to extend the theory given here to allow for $O(a)$ mean-flow velocities as well. This will bring in bottom friction as well as the nonlinear vortex dynamics described in §2. As the mean vorticity grows as $O(a^2 t)$ in the early stage, $O(a)$ mean-flow velocities are achieved over $t = O(a^{-1})$. In principle, an asymptotic theory valid for amplitude-dependent time intervals requires a singular perturbation analysis. However, the present situation seems to be simple enough to arrive at the most important results by inspection, which is what we seek to do now.

For simplicity we will consider only a steady wavetrain. In the early stage we utilized the following scaling assumptions for the mean-flow evolution:

$$t = O(1): \quad \bar{\boldsymbol{u}}^L = O(a^2), \quad \overline{\Delta h} = O(a^2), \quad \frac{\partial}{\partial t} = O(1). \tag{3.40}$$

The first task is to arrive at a later-stage scaling for $\overline{\Delta h}$. Vortices with $\bar{\boldsymbol{u}}^L = O(a)$ require $\overline{\Delta h} = O(|\bar{\boldsymbol{u}}^L|^2) = O(a^2)$ to achieve cyclostrophic balance. Larger, $O(a)$ contributions to $\overline{\Delta h}$ would have to be associated with mean-flow gravity waves, which operate on time scales of $O(1)$. Such waves could perhaps be driven to some extent by unsteady wavetrains. However, they are not likely to interfere significantly with the much slower vortex dynamics, which occurs over an advective, nonlinear time scale $t = O(a^{-1})$. We will hence neglect all mean-flow gravity waves. This can be achieved by the following scaling assumptions for the later-stage mean-flow evolution:

$$t = O(a^{-1}): \quad \bar{\boldsymbol{u}}^L = O(a), \quad \overline{\Delta h} = O(a^2), \quad \frac{\partial}{\partial t} = O(a), \tag{3.41}$$

where the last item fixes the slow, advective time scale for the evolution.

Now, the original linear $O(a)$ waves are not affected by an $O(a)$ mean flow, as their structure depends only on the $O(1)$ background state. Therefore all the equations for $\boldsymbol{u}', h'$ and the wave properties $E, \bar{\boldsymbol{u}}^S, \mathscr{F}$ etc. remain valid in their original form. (Note that we continue to neglect the self-induced shock formation of the shallow-water waves over a time scale $t = O(a^{-1})$. This is possible because of the fixed, $O(1)$ travel time of the waves towards the beach.) As an aside, we note that $\bar{\boldsymbol{u}}^S = O(a^2)$ implies that $|\bar{\boldsymbol{u}}^L| \gg |\bar{\boldsymbol{u}}^S|$ and therefore $\bar{\boldsymbol{u}} \approx \bar{\boldsymbol{u}}^L$ at $O(a)$, i.e. the Stokes drift is now negligible.

Using (3.41) in the continuity equation (3.23) and collecting terms at leading order shows that

$$\nabla \cdot (h_S \bar{\boldsymbol{u}}^L) = 0 \tag{3.42}$$

holds to $O(a)$ (as well as to $O(a^2)$). The manipulation of the mean momentum equation (3.26) is changed only by keeping the term $(\bar{\boldsymbol{u}} \cdot \nabla)\bar{\boldsymbol{u}}$ on the left-hand side and by keeping the friction term from (3.2) on the right-hand side. Abbreviating the friction term by $-\boldsymbol{B}$ and using that $(\bar{\boldsymbol{u}} \cdot \nabla)\bar{\boldsymbol{u}} = (\bar{\boldsymbol{u}}^L \cdot \nabla)\bar{\boldsymbol{u}}^L$ to $O(a^2)$ now, the result is a new version of (3.37) (for a steady wavetrain):

$$\frac{\partial}{\partial t} \nabla \times \bar{\boldsymbol{u}}^L + \nabla \times [(\bar{\boldsymbol{u}}^L \cdot \nabla)\bar{\boldsymbol{u}}^L] = -\nabla \times (\mathscr{F} + \boldsymbol{B}). \tag{3.43}$$

Note that all terms in this equation are $O(a^2)$ by (3.41). Using (3.42) this can be re-written as

$$\left(\frac{\partial}{\partial t} + (\bar{\boldsymbol{u}}^L \cdot \nabla) \right) \left(\frac{\nabla \times \bar{\boldsymbol{u}}^L}{h_S} \right) = -\frac{\nabla \times (\mathscr{F} + \boldsymbol{B})}{h_S}, \tag{3.44}$$

which is also in agreement with a finite-amplitude relation derivable in GLM theory (B2000).

Finally, the bottom friction force term is

$$\boldsymbol{B} = \frac{c_f}{h_S} \overline{|\boldsymbol{u}|\boldsymbol{u}} \tag{3.45}$$

at $O(a^2)$. The nonlinear term $|\boldsymbol{u}|$ makes it hard to write $\boldsymbol{B}$ simply in terms of $\boldsymbol{u}'$ and $\bar{\boldsymbol{u}}^L$. Outside the wavetrain $\boldsymbol{B}$ is simply given in terms of $\bar{\boldsymbol{u}}^L$. Inside the wavetrain one can follow LH70a, b and make the *ad-hoc* assumption that $|\boldsymbol{u}'| \gg |\bar{\boldsymbol{u}}^L|$ and derive an expression for $\boldsymbol{B}$ based on this and on a very simple wave structure; this is detailed in an Appendix. An expression for $\boldsymbol{B}$ valid throughout the domain is then

$$\boldsymbol{B} = \frac{c_f}{h_S} \frac{2}{\pi} u'_{\max} \bar{\boldsymbol{u}}^L \cdot \left(\frac{\boldsymbol{k}\boldsymbol{k}}{\kappa^2} + \boldsymbol{\delta} \right) + \frac{c_f}{h_S} |\bar{\boldsymbol{u}}^L|\bar{\boldsymbol{u}}^L, \tag{3.46}$$

where $u'_{\max} = ac$ is the maximum velocity amplitude of the wave.

Combining (3.42) and (3.44), we see that the slow evolution of the later-stage mean flow does indeed obey the rigid-upper-lid dynamics discussed in detail in §2. The equations derived here allow us to draw fairly definite conclusions about the scaling of the mean-flow behaviour with respect to wave amplitude a. This is very useful, not least because the direct numerical simulations reported in §4 had to be run with very small a. The main observation (as already briefly noted in §2) is that the later-stage mean-flow dynamics (3.42) and (3.44) is symmetric under the scale transformation $a \to \alpha a$ and $t \to \alpha^{-1} t$ for $\alpha > 0$. In other words, the later-stage mean-flow dynamics is self-similar in amplitude a. The early-stage dynamics of both linear waves and mean-flow response is also symmetric, but to a different scale transformation $a \to \alpha a$

and $t \to t$. Finally, the transition time t' from early to later stage scales as $O(a^{-1})$, and hence $t' \to \alpha^{-1} t'$.

An example can now make the overall picture clear. Consider the time evolution of a flow in response to a steady wavetrain with a certain amplitude a. Now consider a second flow in response to the same wavetrain but with twice the amplitude (i.e. $\alpha = 2$). The early-stage mean-flow vorticity forcing in (3.37) will be increased by a factor of four. However, this early stage only lasts half as long now, so that the overall amplitude of the mean-flow has only doubled. The later-stage mean-flow vortex dynamics will hence occur at a doubled amplitude and doubled speed. Therefore, we see that the net effect of doubling the wave amplitude is a doubling of the resultant longshore current velocities.

4. Numerical simulations

We present direct numerical simulations of both waves and vortices in a nonlinear shallow-water model with bottom topography. Our limited aim, at this stage, was to illustrate and cross-check our theoretical predictions for the dynamics of a vortex couple and for current dislocation on barred beaches. Therefore, only highly idealized scenarios (e.g. in terms of topography and shoreline boundary conditions) have been studied, and no claim is made for their quantitative applicability to real beaches, though we believe that this could be achieved in future extensions of this work.

A well-known constraint on shallow-water models in the present context is the self-induced shock formation of waves, which is unrealistic for incoming deep-water waves. This shock formation is rapid (e.g. a wave with amplitude $a = 0.1$ breaks after just a single wavelength of propagation) and it severely limits the wave amplitudes that can be achieved if non-breaking propagation over several wavelengths is desired.

In simulations with homogeneous wavetrains it is possible to overcome this difficulty by moving the seaward boundary and the wavemaker very close to the breaking region (e.g. Kobayashi & Karjadi 1996). However, in our simulations it was essential that the seaward boundary and wave-making region were well separated from the wave-breaking region in order not to interfere with the vortex dynamics there. This explains the necessary use of an unrealistically small wave amplitude $a = 0.015$ below. We suggest that this artificial constraint could be overcome in future work by using a hybrid model that solves the 'modified' shallow-water equations of Bühler (1998) in the deep-water region whilst reverting to the standard equations in the surf zone.

4.1. *Model details*

A shock-resolving finite-volume shallow-water model was used to solve the continuity equation (3.1) and the momentum equation (3.2) in flux form, which is

$$\frac{\partial h\boldsymbol{u}}{\partial t} + \nabla \cdot \left(h\boldsymbol{u}\boldsymbol{u} + \delta \frac{g}{2} h^2 \right) = -gh\nabla h_B + h\nabla\phi_w + h\boldsymbol{F} - c_f |\boldsymbol{u}|\boldsymbol{u}, \tag{4.1}$$

where ϕ_w is a forcing potential for the waves. No explicit dissipative force $\boldsymbol{F}$ was present in the model. However, the model produces dissipation inside the shocks, where the usual hydraulic jump conditions apply to enforce local conservation of mass and momentum. This means that the model behaves as if $\boldsymbol{F} = 0$ in smooth regions, but $\boldsymbol{F} \neq 0$ in shocks (apart from a small amount of numerical diffusion on the grid scale). The upshot is that the model effectively integrates (4.1) with a dissipative force $\boldsymbol{F}$ that is significant only in shocks, where the waves break. Because
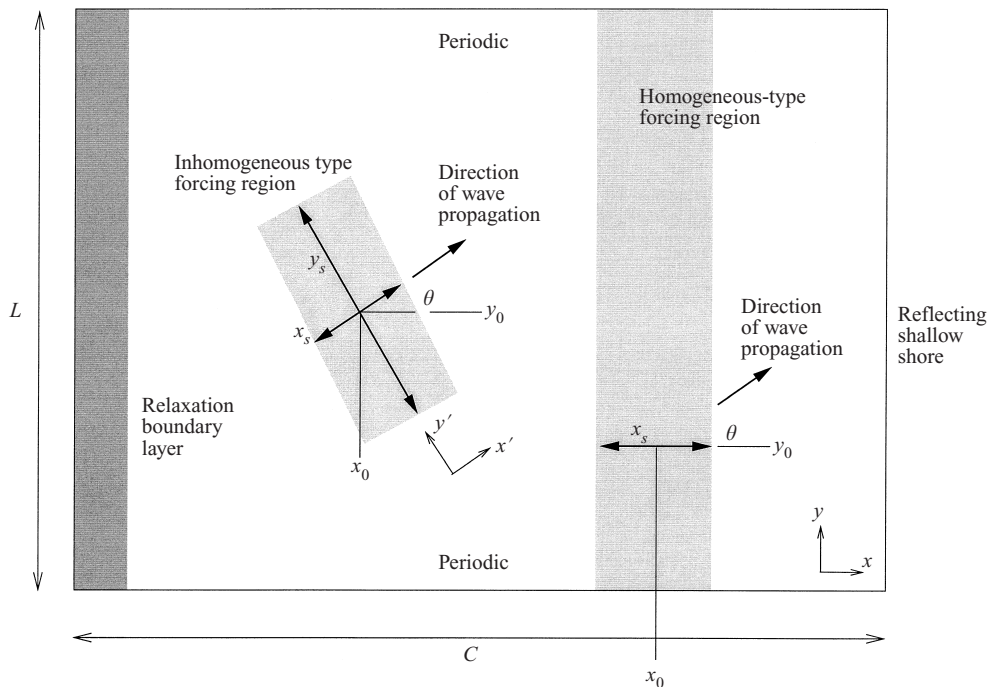
FIGURE 4. A planform of the numerical domain. Note that the forcing centre x_0 has been shifted for ease of presentation even though x_0 was the same in all cases.

F is momentum-conserving, the theory described in §3.3 applies to the numerical integrations.

Because the model resolves the waves, it is quite costly to run long simulations that also capture the mean-flow vortex dynamics, but it was still possible to perform all runs on workstations. The model itself is a slope-limited second-order solver on a uniform Cartesian grid. A Roe-approximate method is used to compute fluxes at cell boundaries. Fluxes for both directions over the entire grid are computed, and the cell values are updated simultaneously over the entire grid at each time step. The bottom topography, bottom friction, and wave forcing are incorporated by a splitting method. A predictor–corrector method ensures that the computation is second-order in time.

A crude radiating boundary was implemented at the seaward edge (where the still water depth is h_{S0}) as a relaxation layer, relaxing the depth to h_{S0} and the velocity to zero. This had no discernible effect on the shoreward-propagating surface waves or on the ensuing vortex dynamics. For simplicity, the other boundary conditions were chosen as periodic in the longshore direction and reflecting at the beach. Indeed, there is no shoreline *per se*, rather the still water depth is made $0.05h_{S0}$ at the shoreward edge to break all but the weakest waves. Whilst convenient and simple, it should be noted that this procedure neglects all effects due to realistic shoreline movement, which is likely to affect the dynamics in the immediate vicinity of the shoreline.

A planform of the model appears in figure 4. The waves are forced by taking the finite-difference gradient of the potential $\phi_w(x,t)$. This makes the forcing approximately curl-free, sidestepping a disruption of the vortex dynamics. The form of the

Parameter	Meaning	Formula or value
CFL	Courant–Friedrichs–Lewys number	0.98
dt	Time step	$\dfrac{\text{CFL}}{\text{wavespeed}}\dfrac{1}{1/dx + 1/dy}\,$s
dx	x grid spacing	1 m
dy	y grid spacing	3 m
C	Cross-shore dimension	200 m
L	Alongshore dimension	498 m
h_{S0}	Still water depth at seaward boundary	4 m
g	Acceleration due to gravity	9.8 m s^{-1}
—	Relaxation rate at seaward damping layer	0.63 s^{-1}
c_f	Bottom friction coefficient used in (3.45)	0.01

TABLE 1. Global model parameters with interpretation and value. The quantity 'wavespeed' in the second row is the maximum shallow-water wavespeed computed at each time step by the program. As a result, dt changes during integration; it is the CFL number which remains constant.)

forcing potential in the inhomogeneous case is

$$\phi_w(\boldsymbol{x}, t) = a\frac{2}{3}\frac{gh_{S0}}{3}R(t)\sin(\omega t)\cos(kx + ly)\cos^2\left(\frac{\pi}{2}\frac{x'}{x_s}\right)\exp\left(-2\left(\frac{y'}{y_s}\right)^2\right). \quad (4.2)$$

This potential generates both a shoreward- and a seaward-propagating wavetrain, which is better behaved numerically than forcing a single wavetrain (cf. Bühler & McIntyre 1998). The seaward-propagating waves are absorbed at the seaward boundary. Here x_s, y_s are the envelope scales and x', y' are local coordinates measured from the wave-forcing centre x_0, y_0. The waves propagate at an angle $\theta = \arctan(l/k)$, and in the inhomogeneous case the local coordinates were in fact rotated by θ, as shown in figure 4. The function $R(t)$ represents a smooth ramp function which is turned on at $t = 0$ and saturates to unity within a couple of wave periods.

In the homogeneous case there is no alongshore envelope, and the forcing potential is (4.2) without the last term and with x'/x_s replaced by x/x_s. In both cases the forcing potential is zero outside the forcing region indicated by the shaded boxes in figure 4. Global model parameters are listed in table 1 along with their associated values. The wavelength for the simulations was chosen by balancing numerical cost against the requirement of achieving a spatial scale separation between waves and mean fields (note that the ray-tracing theory in §3.2 showed that the effective dissipative force $-\mathscr{F}$ does not depend on the wavelength). We found that about 20 grid points per wavelength were required to resolve a propagating wave without excessive numerical diffusion. The choices for all the wave parameters are summarized in table 2.
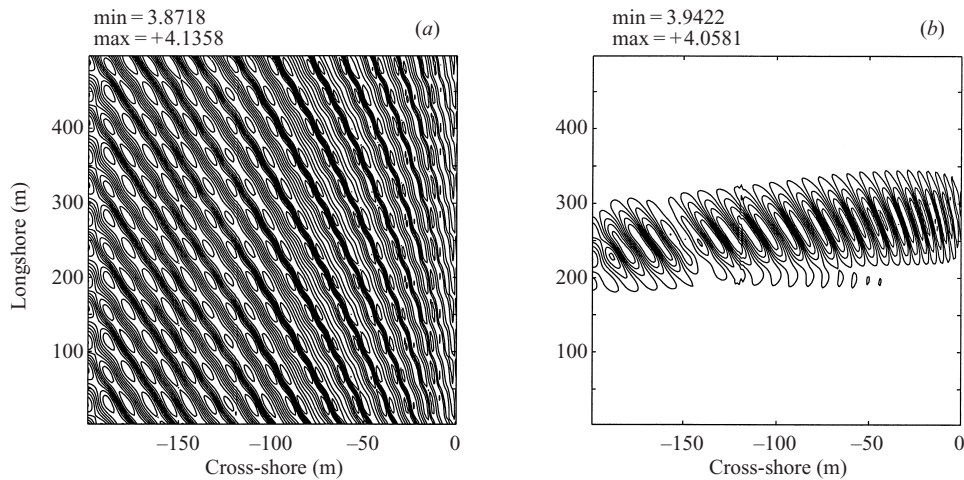
4.2. *Planar beach*

To prepare for the barred-beach simulations the scheme was first tested on a simple planar beach, with profile $h_B(x)$ chosen as two straight lines: $h_B = 0$ for $x < -125$ m, whilst for $x > -125$ m h_B grows linearly to $h_B = 0.95h_{S0} = 3.8$ m at the shoreline $x = 0$. Typical images of homogeneous and inhomogeneous wavetrains respectively are shown in figure 5. These illustrate the refraction as well as the amplitude decay due to shock-induced dissipation. They also show that the discontinuous topography slope at $x = -125$ m leads to some weak numerical oscillations there.

In figure 6 we look at the evolution of the Eulerian-mean longshore current, which

Parameter	Meaning	Value (Homogeneous)	Value (Homogeneous)
a	Amplitude of forced waves	0.015	0.015
θ	Angle of incidence	15°	15°
κ	Magnitude of wavenumber vector	$0.2913\,\mathrm{m}^{-1}$	$0.3034\,\mathrm{m}^{-1}$
λ	Wavelength $= 2\pi/\kappa$	21.56 m	20.70 m
ω	Forcing frequency $= \sqrt{gh_{S0}}\,\kappa$	$1.82\,\mathrm{s}^{-1}$	$1.90\,\mathrm{s}^{-1}$
x_0	Cross-shore centre of wave forcing	-150 m	-150 m
y_0	Alongshore centre of wave forcing	250 m	250 m
x_s	Envelope scale for ϕ_w	λ	λ
y_s	Envelope scale for ϕ_w	∞	3λ

TABLE 2. Wave parameters, interpretation and value.

FIGURE 5. Layer height $h + h_B$ after 200 wave periods on a planar beach with bottom friction: (*a*) homogeneous wavetrain; (*b*) inhomogeneous wavetrain. The weak impact of the discontinuous topography slope can be made out at $x = -125$ m.

is defined as the y-averaged alongshore velocity v. (The mean velocity scales as $O(a)$ in the later, friction-controlled stage (cf. LH70*a, b* and §3.5 here) and hence Stokes corrections (which are $O(a^2)$) become negligible then. Therefore, one can note that $\bar{u}$ and $\bar{u}^L$ are approximately equal at this stage.) The wave breaking extends all the way to the shoreline on this beach, and in response we see the build-up and saturation of a broad current in the homogeneous case in (*a*). In accordance with LH70*a, b*, the current maximum forms roughly at the onset of wave breaking. The current does not go to zero at the shoreline boundary because of the finite water depth and reflecting boundary condition there. There is also a spurious weak counter-current near the sea-side boundary condition, which has been forced by the weak dissipation of the seaward-going wavetrain generated by the wavemaker at $x = -150$ m.

The longshore current in the inhomogeneous case in figure 6(*b*) is much weaker, by a factor of about 20. This is explained in part by the Gaussian wavetrain envelope in (4.2), which in the present case reduces the wave-induced influx of y-momentum by a factor of about 5. Also, the depicted longshore current is now the y-average over an inhomogeneous, slowly varying mean flow, a significant part of which lies outside the
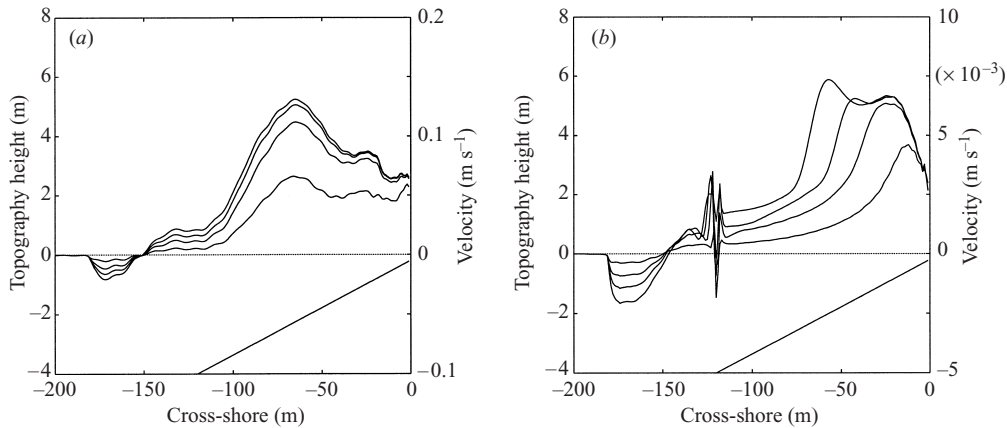
FIGURE 6. Growing longshore currents after 200, 500, 800, and 1200 wave periods on a planar beach with bottom friction. The bottom topography is also depicted. y-averaged alongshore velocity v for (*a*) a homogeneous wavetrain, and (*b*) an inhomogeneous wavetrain, with strongly reduced amplitude scale.

wavetrain. This means that the scaling of LH70*a*,*b* for the bottom friction term does not apply in this case, and so there is no obvious link between incoming momentum flux and current peak amplitude in the inhomogeneous case.

The weaker current amplitude also makes obvious the numerical oscillations caused by the discontinuous topography slope at $x = -125$ m. This emphasize the importance of a continuous topography slope, which we took care to observe in the barred-beach simulations below.

4.3. *Barred beach*

A very simple topography profile $h_B(x)$ with continuous slope was chosen here:

$$\frac{h_B(x)}{h_{S0}} = \begin{cases} 0, & x < -120 \\ 0.75\sin^2(\pi(x+120)/40), & -120 < x < -100 \\ 0.5 + 0.25\cos^2(\pi(x+100)/100), & -100 < x < -50 \\ 0.5 + 0.45\sin^2(\pi(x+50)/100), & -50 < x < 0, \end{cases} \quad (4.3)$$

where x is in m and $h_{S0} = 4$ m. So, the bar crest rises sharply to 75% of h_{S0} at $x = -100$ m, then falls to 50% in the trough at $x = -50$ m, before rising again to 95% at the shoreline $x = 0$. No detailed similarity with a real beach was intended, though these numbers were roughly motivated by the topography encountered in the observations at Duck, North Carolina (e.g. Church & Thornton 1993).

The wave breaking now occurs mainly over the bar crest at $x = -100$ m, with a weaker secondary breaking region near the shoreline. The dynamics of a vortex couple on this beach is displayed in a sequence of PV images in figure 7. In order to show the vortex dynamics most clearly, this particular simulation was performed without bottom friction, i.e. $c_f = 0$ in this run only. Also, the region $x > -30$ m nearest to the shoreline is not shown because of the very large PV values there (due to the factor $1/h$ in (3.3)) and also because of the noted sensitivity of this region to the shoreline boundary condition.

The panels very clearly show three distinct phases in the vortex couple evolution: growth over the bar crest, propagation towards the shoreline, and finally separation
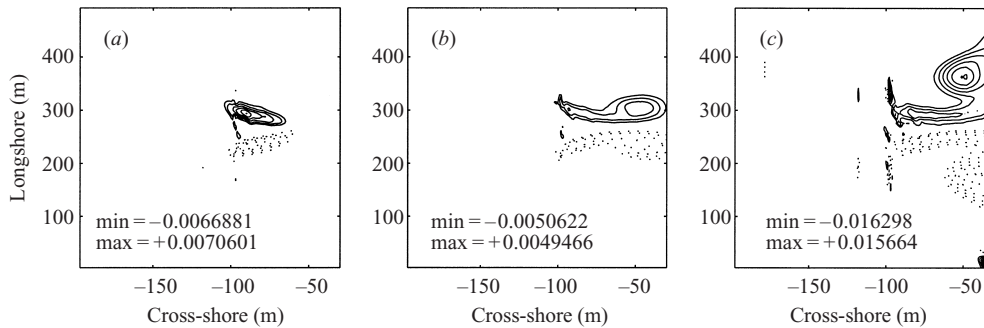
FIGURE 7. PV contours for $x < -30$ m after (a) 200, (b) 500, and (c) 800 wave periods on a barred beach without bottom friction. Solid or dotted contours correspond to positive or negative PV, respectively.
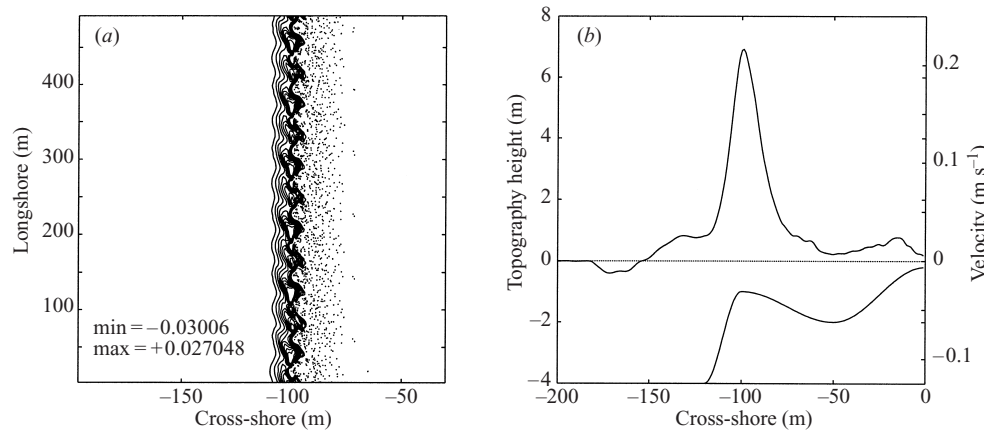

FIGURE 8. Simulations with a homogeneous wavetrain after 1200 wave periods on a barred beach with bottom friction. (a) PV contours for $x < -30$ m. Solid or dotted contours correspond to positive or negative PV, respectively. (b) y-averaged alongshore velocity v.

along the shore. This is in good agreement with the theoretical expectations discussed earlier.

Finally, we show simulations with bottom friction, aiming at a saturated, nearly steady state for the barred beach. The results for homogeneous and inhomogeneous wavetrains are displayed in figure 8 and figure 9, respectively, which are both taken after 1200 wave periods. In accordance with LH70a,b, the homogeneous case shows a clearly defined, quite narrow current located over the bar crest, where most of the wave breaking occurs. There is also a weaker secondary peak at the shoreline, where the remaining wave breaking occurs, and, as before, there is a spurious counter-current near the seaward boundary condition.

In the inhomogeneous case in figure 9, however, there is a much broader current (again, with much reduced amplitude) now located over the bar trough instead of the bar crest. This appears to be a clear example of possible current dislocation due to the dynamics of a vortex couple that is forced by an inhomogeneous wavetrain.

In summary, we have illustrated with idealized simulations how vortex dynamics and concomitant current dislocation effects can play a significant rôle on barred beaches when inhomogeneous wavetrains are considered. As noted before, future
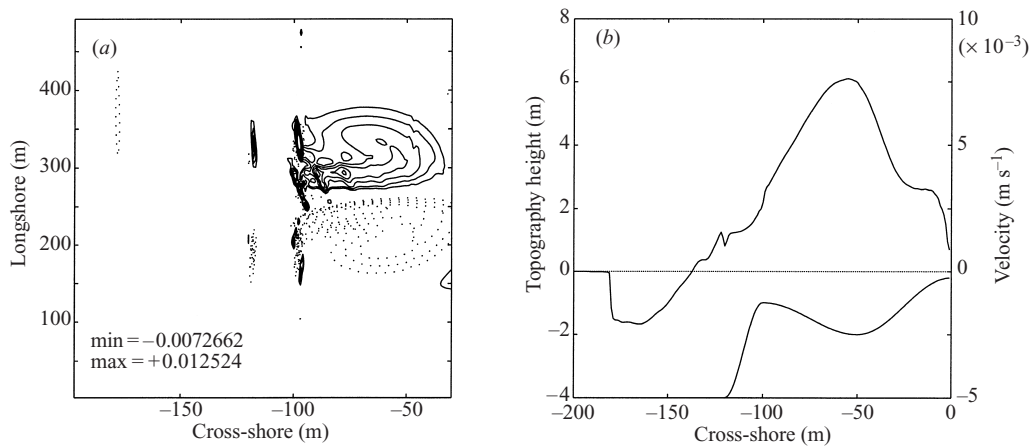
FIGURE 9. Simulations with an inhomogeneous wavetrain after 1200 wave periods on a barred beach with bottom friction. (*a*) PV contours for $x < -30$ m. Solid or dotted contours correspond to positive or negative PV, respectively. (*b*) *y*-averaged alongshore velocity v. (Note the reduced amplitude scale.)

direct numerical simulations of less idealized scenarios will require an improved treatment of the deep-water waves and of the shoreline boundary condition. Such direct numerical simulations should be useful to guide the design of models for the vortex dynamics only, in which the inhomogeneous wavetrain dynamics (including wave breaking) is parametrized.

5. Concluding remarks

We have introduced a new mechanism based on vortex dynamics that offers a possible explanation for current dislocation on barred beaches. The main restriction was that we only considered a single wavetrain, or several well-separated wavetrains. However, many partially overlapping wavetrains seem to be the norm on real surf zones. This might lead to near-cancellation of vortex couples, and hence to a strongly diminished capacity for the type of coherent vortex propagation that was envisaged in the present paper. A study that generalizes our work to apply in such a situation would be extremely valuable.

From a fundamental theoretical point of view, a study of this kind may require the development of a theory of forced–dissipative two-dimensional turbulence on a sloping beach. It would certainly be interesting to see whether typical two-dimensional turbulence features such as vortex mergers and the concomitant up-scale evolution of energy will also arise on a sloping beach. This would also address the open problem of whether selective decay due the factor h_S^{-1} in the bottom friction term would make the bar trough a preferred vortex location. We are unaware of fundamental studies of these problems to date. We have noted that in the absence of forcing and dissipation some progress can be made on a statistical theory of vortices on a sloping beach along the lines of Onsager's original theory for point vortices. Work is currently being pursued in this direction.

From a numerical point of view, one result of the costly direct numerical simulations presented here was to verify that the wave dynamics was only weakly affected by the mean-flow dynamics. This means that a fruitful numerical research direction is to run a shallow-water model with a rigid upper lid (as in §2) that is forced by an

effective dissipative force $-\mathscr{F}$ via (3.44). Here $\mathscr{F}$, $\boldsymbol{p}$ and $\boldsymbol{B}$ could be modelled by the ray-tracing theory detailed in §3.2. This would allow time-stepping on the advective time scale $t = O(a^{-1})$, which would reduce the number of time steps by two orders of magnitude. This should be enough to allow a numerical study of a surf zone with many wavetrains, even with a two-dimensional $h_S(x, y)$. As this requires a completely different numerical code, we have not yet pursued work in this direction.

We note in passing that fundamental theoretical and numerical work on two-dimensional turbulence in slanted, wedge-shaped domains is also of general interest outside coastal oceanography. For instance, there appear to be related problems to do with vortex dynamics in gravitating astrophysical accretion disks, which can have a pronounced slanted geometry (E. A. Spiegel, personal communication).

Finally, we note that the great practical usefulness of the LH70*a, b* theory is rooted in the fact that it allows the simple analytical computation of an average profile for the longshore current. Such a simple computational method for finding the mean current is lost once mean-flow vortices are recognized as playing a significant rôle. For instance, the work presented here shows clearly that the dynamics of these vortices cannot be modelled by eddy diffusion. Future advances in understanding the average dynamics of these vortices may lead to a new, but again simple, computational method for calculating the averaged longshore current on barred beaches.

Appendix

A.1. *Derivation of* (3.14)

After multiplying (3.6) with h'/h_S, averaging and using (3.5) we obtain

$$\frac{\partial \bar{\boldsymbol{u}}^S}{\partial t} + \frac{1}{h_S} \overline{\boldsymbol{u}' \nabla \cdot (h_S \boldsymbol{u}')} + \frac{g}{2h_S} \nabla \overline{h'^2} = \frac{1}{h_S} \overline{h' \boldsymbol{F}'}. \tag{A 1}$$

The second term can be re-written exactly as

$$\frac{1}{h_S} \overline{\boldsymbol{u}' \nabla \cdot (h_S \boldsymbol{u}')} = \frac{1}{h_S} \nabla \cdot (h_S \overline{\boldsymbol{u}' \boldsymbol{u}'}) - \overline{(\boldsymbol{u}' \cdot \nabla) \boldsymbol{u}'} \tag{A 2}$$

$$= \frac{1}{h_S} \nabla \cdot (h_S \overline{\boldsymbol{u}' \boldsymbol{u}'}) - \tfrac{1}{2} \nabla \overline{|\boldsymbol{u}'|^2} + \overline{\boldsymbol{u}' \times \hat{\boldsymbol{z}} (\nabla \times \boldsymbol{u}')} \tag{A 3}$$

$$= \frac{1}{h_S} \nabla \cdot (h_S \overline{\boldsymbol{u}' \boldsymbol{u}'}) - \tfrac{1}{2} \nabla \overline{|\boldsymbol{u}'|^2} + \frac{\partial}{\partial t} (\overline{\boldsymbol{\xi}' \times \hat{\boldsymbol{z}} (\nabla \times \boldsymbol{u}')}) - \overline{\boldsymbol{\xi}' \times \hat{\boldsymbol{z}} (\nabla \times \boldsymbol{F}')}, \tag{A 4}$$

where the last line uses (3.8) and (3.7). Substituting (A 4) back in (A 1), using (3.12) and (3.12) with u'_j replaced by F'_j finally gives (3.14).

A.2. *Derivation of* (3.46)

Outside the wavetrain $u' = 0$ and hence the last term in (3.46) is obtained. Inside the wavetrain we assume that $|u'| \gg |\bar{u}^L|$ and $|u'| \gg |\bar{u}|$ and that

$$u' = \frac{k}{\kappa} ac \sin \theta \quad \text{with phase } \theta \in [0, 2\pi]. \tag{A 5}$$

In general, we have

$$|u| = |\bar{u}| + |u|', \quad \overline{|u|u} = |\bar{u}|\,\bar{u} + \overline{|u|u'}, \tag{A 6}$$

due to $\overline{|\bar{u}|u'} = 0$. The nonlinear term $|u|$ is

$$|u| = \sqrt{|u'|^2 + 2u' \cdot \bar{u} + |\bar{u}|^2} \approx |u'| + \frac{u' \cdot \bar{u}}{|u'|} \tag{A 7}$$

after expanding the root. Combining (A 5)–(A 7) and $\overline{|\sin \theta|} = 2/\pi$ then produces the first term in (3.46) with $\bar{u}^L$ replaced by $\bar{u}$. Using that $a\bar{u} = a\bar{u}^L + O(a^3)$ then allows replacing $\bar{u}$ by $\bar{u}^L$ whilst retaining $O(a^2)$ accuracy.

REFERENCES

ANDREWS, D. G., HOLTON, J. R. & LEOVY, C. B. 1987 *Middle Atmosphere Dynamics*. Academic.

ANDREWS, D. G. & MCINTYRE, M. E. 1978 An exact theory of nonlinear waves on a Lagrangian-mean flow. *J. Fluid Mech.* **89**, 609–646.

BÜHLER, O. 1998 A shallow-water model that prevents nonlinear steepening of gravity waves. *J. Atmos. Sci.* **55**, 2884–2891.

BÜHLER, O. 2000 On the vorticity transport due to dissipating or breaking waves in shallow-water flow. *J. Fluid Mech.* **407**, 235–263 (referred to herein as B2000).

BÜHLER, O. & MCINTYRE, M. E. 1998 On non-dissipative wave–mean interactions in the atmosphere or oceans. *J. Fluid Mech.* **354**, 301–343.

CHURCH, J. C. & THORNTON, E. B. 1993 Effects of breaking wave induced turbulence within a longshore current model. *Coastal Engng* **20**, 1–28.

KOBAYASHI, N. & KARJADI, E. A. 1996 Obliquely incident irregular waves in surf and swash zones. *J. Geophys. Res.* **101** (C3), 6527–6542.

LAMB, H. 1932 *Hydrodynamics*, 6th Edn. Cambridge University Press.

LONGUET-HIGGINS, M. S. 1970a Longshore currents generated by obliquely incident sea waves 1. *J. Geophys. Res.* **75**, 6778–6789 (referred to herein as LH70a).

LONGUET-HIGGINS, M. S. 1970b Longshore currents generated by obliquely incident sea waves 2. *J. Geophys. Res.* **75**, 6790–6801 (referred to herein as LH70b).

LONGUET-HIGGINS, M. S. & STEWART, R. W. 1960 Changes in the form of short gravity waves on long waves and tidal currents. *J. Fluid Mech.* **8**, 565–583.

LONGUET-HIGGINS, M. S. & STEWART, R. W. 1961 The changes in amplitude of short gravity waves on steady non-uniform currents. *J. Fluid Mech.* **10**, 529–549.

LONGUET-HIGGINS, M. S. & STEWART, R. W. 1962 Radiation stress and mass transport in gravity waves, with application to 'surf beats'. *J. Fluid Mech.* **13**, 481–504.

LONGUET-HIGGINS, M. S. & STEWART, R. W. 1963 A note on wave set-up. *J. Mar. Res.* **21**, 4–10.

LONGUET-HIGGINS, M. S. & STEWART, R. W. 1964 Radiation stress in water waves; a physical discussion, with applications. *Deep-sea Res.* **11**, 529–562.

PEREGRINE, D. H. 1998 Surf zone currents. *Theor. Comput. Fluid Dyn.* **10**, 295–310.

PEREGRINE, D. H. 1999 Large-scale vorticity generation by breakers in shallow and deep water. *Eur. J. Mech.* B/*Fluids* **18**, 403–408.

RENIERS, A. J. H. M. & BATTJES, J. A. 1997 A laboratory study of longshore currents over barred and non-barred beaches. *Coastal Engng* **30**, 1–22.

RICHARDSON, G. 2000 Vortex motion in shallow water with varying bottom topography and zero Froude number. *J. Fluid Mech.* **411**, 351–374.

THORPE, S. A. & CENTURIONI, L. R. 2000 On the use of the method of images to investigate nearshore dynamical processes. *J. Mar. Res.* **58**, 779–788.